The rising light curves of Type Ia supernovae

R. E. Firth,[1]★ M. Sullivan,[1] A. Gal-Yam,[2] D. A. Howell,[3] K. Maguire,[4] P. Nugent,[5,6]
A. L. Piro,[7] C. Baltay,[8] U. Feindt,[9] E. Hadjiyksta,[8] R. McKinnon,[8] E. Ofek,[2]
D. Rabinowitz[8] and E. S. Walker[8]

[1]*School of Physics and Astronomy, University of Southampton, Southampton SO17 1BJ, UK*
[2]*Benoziyo Center for Astrophysics, Weizmann Institute of Science, 76100 Rehovot, Israel*
[3]*Las Cumbres Observatory Global Telescope Network, Goleta, CA 93117, USA*
[4]*European Southern Observatory, Karl-Schwarzschild-Str. 2, D-85748 Garching bei München, Germany*
[5]*Computational Cosmology Center, Lawrence Berkeley National Laboratory, 1 Cyclotron Road, Berkeley, CA 94720, USA*
[6]*Department of Astronomy, University of California, Berkeley, CA 94720-3411, USA*
[7]*Theoretical Astrophysics, California Institute of Technology, 1200 E California Boulevard, M/C 350-17, Pasadena, CA 91125, USA*
[8]*Department of Physics, Yale University, New Haven, CT 06250-8121, USA*
[9]*Physikalisches Institut, Universität Bonn, Nußallee 12, D-53115 Bonn, Germany*

ABSTRACT

We present an analysis of the early, rising light curves of 18 Type Ia supernovae (SNe Ia) discovered by the Palomar Transient Factory and the La Silla-QUEST variability survey. We fit these early data flux using a simple power law ($f(t) = \alpha \times t^n$) to determine the time of first light (t_0), and hence the rise time (t_{rise}) from first light to peak luminosity, and the exponent of the power-law rise (n). We find a mean uncorrected rise time of 18.98 ± 0.54 d, with individual supernova (SN) rise times ranging from 15.98 to 24.7 d. The exponent n shows significant departures from the simple 'fireball model' of $n = 2$ (or $f(t) \propto t^2$) usually assumed in the literature. With a mean value of $n = 2.44 \pm 0.13$, our data also show significant diversity from event to event. This deviation has implications for the distribution of ^{56}Ni throughout the SN ejecta, with a higher index suggesting a lesser degree of ^{56}Ni mixing. The range of n found also confirms that the ^{56}Ni distribution is not standard throughout the population of SNe Ia, in agreement with earlier work measuring such abundances through spectral modelling. We also show that the duration of the very early light curve, before the luminosity has reached half of its maximal value, does not correlate with the light-curve shape or stretch used to standardize SNe Ia in cosmological applications. This has implications for the cosmological fitting of SN Ia light curves.

Key words: supernovae: general.

1 INTRODUCTION

Type Ia supernovae (SNe Ia) are bright stellar explosions that can be standardized and used as distance indicators over cosmic scales. Relative distances calculated using SNe Ia were used to uncover the accelerating expansion of the Universe (Riess et al. 1998; Perlmutter et al. 1999), and, more recently in the era of large surveys, sufficient accuracy has been attained to enable precise cosmological measurements (Kessler et al. 2009; Sullivan et al. 2011; Suzuki et al. 2012; Betoule et al. 2014; Rest et al. 2014).

SNe Ia are thought to be the result of a thermonuclear explosion of a carbon–oxygen (CO) white dwarf (WD) star as a result of mass

transfer to the WD in a binary system. This is supported by recent observations placing constrains on the radius of the progenitor, consistent with a WD (Nugent et al. 2011; Bloom et al. 2012). Two basic scenarios for the progenitor systems are generally considered: single-degenerate systems (Whelan & Iben 1973), comprising a WD accompanied by a less evolved secondary, and double-degenerate (DD) systems (Iben & Tutukov 1984) with two WDs. Other variations on these two scenarios include the detonation of a helium shell on a CO WD that leads to core detonation (double detonation) (Woosley & Weaver 1994; Livne & Arnett 1995; Shen & Bildsten 2014), the triggering of dynamical burning during the DD tidal disruption itself (Pakmor et al. 2012), and collisions between two WDs in a triple system (Katz & Dong 2012; Kushnir et al. 2013). Whatever the mechanism, as the progenitor WD's mass increases and approaches the Chandrasekhar mass, M_{ch}, carbon burning is ignited

★ E-mail: r.firth@soton.ac.uk

and a runaway thermonuclear explosion results (in the collisional and double-detonation cases, the total mass may not need to reach M_{ch} due to additional compression forces). However, many of the exact physical details behind this picture are poorly understood (see the recent review of Maoz, Mannucci & Nelemans 2014).

Studying SNe Ia just after their explosion is important for understanding the physics of the ejected material. Immediately following the explosion, a shock travels through the envelope, causing it to become unbound from the star. In the case where the shock is radiation dominated, the shock travels outwards until the optical depth falls to a level at which the radiation driving the shock can escape as a UV/X-ray flash. The shock breakout of the explosion itself is likely too dim and fast to be detectable for extragalactic events (Nakar & Sari 2012; Rabinak, Livne & Waxman 2012), but emission from the cooling ejecta heated by the shock could be detected. This shock-heated cooling is predicted to be faint but should be best observed in UV and blue optical bands (Piro & Nakar 2013). Adding to the difficulty in detection, the time-scale for this faint emission is very short given the small size of the progenitor star (Piro, Chang & Weinberg 2010; Nugent et al. 2011; Bloom et al. 2012). Other sources of very early emission could trace the presence of companion stars. For instance, if the ejecta collides with a companion it may cause a disruption and re-heating of the ejecta, as well as blowing a hole in the ejecta, where high-energy emission could escape (Kasen 2010). However, optical searches for this effect have so far been unsuccessful (Hayden et al. 2010b; Bianco et al. 2011). Another possible source of emission may arise from the SN Ia ejecta interacting with shells of circumstellar material (CSM) previously ejected by the system (Patat et al. 2007).

Interaction can occasionally be seen in the spectra of a supernova (SN) either through absorption or emission. The strongest emission lines have been seen in SNe Ia initially misclassified as SNe IIn due to strong Hα emission (Silverman et al. 2013) and have been termed SNe Ia-CSM. This emission arises by conversion of the kinetic energy of the fast-moving SN ejecta into radiation by shock interaction with a slow-moving CSM.

However, the bulk of the early optical light curve of an SN Ia is powered by the radioactive decay of ^{56}Ni ($\rightarrow$ ^{56}Co $\rightarrow$ ^{56}Fe) synthesized in the explosion (Hoyle & Fowler 1960; Colgate & McKee 1969; Arnett 1982; Pinto & Eastman 2000a), and thus the shape of the light curve gives clues as to the distribution of the ^{56}Ni in the ejecta. The first photons that diffuse out of the ejecta result from energy deposition from the decay of the ^{56}Ni that is located furthest out in the ejecta (Piro & Nakar 2013). This process is not instantaneous, and as such, there may be a dark phase between explosion and first light, as has recently been implied by abundance tomography (Hachinger et al. 2013; Mazzali et al. 2014). The escape of the first photons starts the rise of the light curve, and as the ejecta expands, photons generated by energy deposited by deeper ^{56}Ni escape. The expanding ejecta become less opaque, increasing the amount of energy escaping, and the point at which the energy radiated is equal to the energy deposited by ^{56}Ni is identifiable as a point of inflection on the light curve (Pinto & Eastman 2000a). The ejecta continue to radiate previously deposited energy as well as the energy instantaneously deposited by ongoing ^{56}Ni decays, and consequently the peak of the SN light curve occurs several days later. The time between the first photons escaping the ejecta (not necessarily the time of explosion) and this peak is the 'rise time', with a value of $\sim$17.5 d to *B*-band peak for a normal SN Ia event (Hayden et al. 2010b).

Although SNe Ia show considerable variation in their peak brightness from event to event, they are ultimately standardizable (Phillips

Table 1. Rise-time results from the literature.

Survey	n	Rise time (d)
SDSS[a]	$1.8^{+0.23}_{-0.18}$	17.38 ± 0.17
LOSS[b]	$2.2^{+0.27}_{-0.19}$	18.03 ± 0.24
SNLS[c]	$1.92^{+0.31}_{-0.37}$	$16.85^{+0.54}_{-0.81}$

[a]Hayden et al. (2010a), [b]Ganeshalingam et al. (2011), and [c]González-Gaitán et al. (2012).

1993) in the sense that brighter SNe Ia have slower evolving light curves. This is usually parametrized by either a stretch-like parameter (e.g. Perlmutter et al. 1997; Guy et al. 2007), often denoted x_1, which measures the speed of an SN Ia relative to a normal event, or a Δm-like parameter, which measures the rate at which a light curve fades after peak brightness (Phillips 1993; Riess, Press & Kirshner 1996).

The width of the bolometric light curve of an SN Ia is related to the photon diffusion time (Pinto & Eastman 2000b; Woosley et al. 2007). A photon emitted in a ^{56}Ni decay will random walk out of the ejecta, depositing energy at each collision. A longer diffusion time means that the photon spends longer within the ejecta and as such deposits more energy in total, both increasing the peak brightness and stretching the light curve. The important parameters for determining the bolometric diffusion time are the mass of the ejecta, the kinetic energy, the radial distribution of ^{56}Ni and the effective opacity (Woosley et al. 2007). The opacity increases with the ionization state of Fe-group elements, which blanket the blue, and, as this increases with temperature, links opacity to the ^{56}Ni mass – as hotter, brighter SNe Ia have more ^{56}Ni.

The study of SN Ia rise times has a long history (Pskovskii 1984; Riess et al. 1999; Conley et al. 2006; Strovink 2007; Hayden et al. 2010a; Ganeshalingam, Li & Filippenko 2011; González-Gaitán et al. 2012). Pskovskii (1984) used 54 literature SNe Ia to demonstrate a range in rise-time values, with the rise time correlating with the decline rate over 100 d. Riess et al. (1999) used 30 unfiltered CCD observations and data at an earlier epoch than previously available, and measured $t_{rise} = 19.5 \pm 0.2$ d. They found that the rise time was correlated with peak luminosity in the sense that longer rise times were found in brighter SNe, as expected if the speed of the early light curve correlates with the light-curve shape.

More recent work has used high-redshift SN surveys such as the Supernova Legacy Survey (SNLS; Astier et al. 2006) and the Sloan Digital Sky Survey (SDSS) SN search (Frieman et al. 2008). These surveys achieve a large sample size with very early detections due to their large search volume, time-dilated SN light curves, and high-cadence repeat imaging of 'blank' areas of sky. Lower redshift surveys, such as the Lick Observatory Supernova Search (LOSS; Li et al. 2000) that targeted nearby luminous galaxies, obtained a higher signal-to-noise ratio (S/N), but located fewer SNe due to a smaller search volume. These surveys extract a rise time from their SNe by correcting all the SNe to the same peak brightness and light-curve width, and using a single rise-time value to represent the resulting distributions (Conley et al. 2006; Hayden et al. 2010a; Ganeshalingam et al. 2011; González-Gaitán et al. 2012). These studies were also able to investigate the shape of the early light curve, parametrizing the early luminosity evolution as a power law with exponent n. They generally found values of n consistent with 2 (i.e. a light-curve evolution proportional to t^2), and the results of these studies are summarized in Table 1.

Some subtleties have emerged. Using eight well-sampled SNe Ia corrected for light-curve width, Strovink (2007) found a range of rise times with a dispersion of $0.96^{+0.52}_{-0.25}$ d, and some evidence for a bimodal distribution. Ganeshalingam et al. (2011) and Hayden et al. (2010a) use 'two-stretch' models to fit stretches to the rising and falling sections of the light curves separately. Ganeshalingam et al. (2011) note that the rise time of high-stretch SNe Ia is shorter than would be expected based on the rest of their light-curve shape.

A handful of well-sampled, high-S/N local SNe Ia, in some cases discovered just a few hours after first light, have sufficient data to individually constrain the rise-time exponent (n): SN 2011fe, $n = 2.01 \pm 0.01$ (Nugent et al. 2011); SN 2010jn, $n = 2.3 \pm 0.6$ (Hachinger et al. 2013); SN 2013dy, $n = 2.24 \pm 0.08$ (Zheng et al. 2013); and SN 2014J, 2.94 ± 0.20 (Goobar et al. 2014; Zheng et al. 2014). All of these studies found $n \geq 2$. Such early time data are particularly valuable for placing constraints on the progenitor (Nugent et al. 2011) and the physical processes within the ejecta (Piro & Nakar 2013).

In this paper, we use 18 SN Ia discoveries from two low-redshift SN surveys: the Palomar Transient Factory (PTF; Law et al. 2009; Rau et al. 2009), and the La Silla-QUEST Variability Survey (LSQ; Baltay et al. 2013). Both surveys operate with a similar 1–3 d cadence, and are wide-area rolling searches. This ensures that the early SN light curves are well sampled, with strong constraints on the SN first light. This also means that, rather than calculating an average rise time for the survey ensemble, individual events can be fitted both for the rise time and the exponent of the power-law rise. We consider how the light curve behaves at these early times, what this can tell us about the physical conditions in the ejecta, and how this may relate to the progenitor. We also investigate the subclass of SNe Ia-CSM (Silverman et al. 2013) to establish to what extent their rises are consistent with 'normal' SNe Ia.

The plan of the paper is as follows. In Section 2, we present the SN Ia data used in our analysis and our sample of 18 SNe Ia. Section 3 contains a review of the parametrizations of the early time light curves of SNe Ia, and the methods applied to fit them to the data. Section 4 presents the results of our study of a sample of 18 'normal' SNe Ia, and in Section 5 these results are discussed, along with SNe Ia-CSM.

2 DATA

In this section, we introduce the sources of the SN data used in this paper, the SN photometry, and the selection of the events that we use for our analysis sample.

2.1 The supernova surveys

Our data come from two local, rolling SN surveys. The first is the PTF (Law et al. 2009; Rau et al. 2009), a wide-field survey using the CFH12k camera mounted on the 48 inch Samuel Oschin telescope at Palomar Observatory (the P48 telescope). The survey operated primarily in an R-band filter (hereafter R_{P48}), with occasional runs in a g filter (g_{P48}) around new moon. The cadence varied between a few hours and 5 d, although after selection cuts all the data in this paper have a cadence of 4 d or better, and each 60 s exposure typically reached a depth of $R_{P48} \approx 21$. The combination of depth and cadence enabled the discovery of around 1250 spectroscopically confirmed SNe Ia (e.g. Pan et al. 2014). The PTF images were processed by the PTF/IPAC pipeline described in Laher et al. (2014) and are photometrically calibrated (Ofek et al. 2012a).

The second survey is the LSQ (Baltay et al. 2013), a Southern Hemisphere variability survey using the 10 deg^2 QUEST instrument (Baltay et al. 2007) on the 1.0 m European Southern Observatory Schmidt telescope at La Silla, Chile. LSQ operates with a cadence of between 2 h and 2 d, using a broad gr filter (hereafter gr_{LSQ}).

The SNe in this paper were spectroscopically confirmed using the Palomar Observatory Hale 200 inches and the double spectrograph, the William Herschel Telescope and the Intermediate dispersion Spectrograph and Image System, the Keck-I telescope and the Low-Resolution Imaging Spectrometer (Oke et al. 1995), the Keck-II telescope and the Deep Imaging Multi-Object Spectrograph (Faber et al. 2003), the Lick Observatory 3 m Shane telescope and the Kast Dual Channel Spectrograph (Miller & Stone 1994), the Gemini-N telescope and the Gemini Multi-Object Spectrograph (Hook et al. 2004) and the University of Hawaii 88 inches and the Supernova Integral Field Spectrograph (Lantz et al. 2004).

All of the classification spectra for SNe in this paper are available via the WISeREP archive (Yaron & Gal-Yam 2012), and are also presented in Maguire et al. (2014).

2.2 SN photometry

Our photometric light curves originate from the original SN searches. We use a single pipeline written by one of us (MS) to construct all of the light curves from both PTF and LSQ. This pipeline has been used extensively in earlier PTF papers (e.g. Maguire et al. 2012; Ofek et al. 2013, 2014a; Pan et al. 2014) and we summarize the main details here.

The photometric pipeline runs on image subtraction, constructing a deep reference image from data prior to the SN explosion, registering this reference to each image containing the SN light, matching the point spread functions (PSFs), performing image subtraction, and then measuring the SN flux using PSF photometry on the difference images. The PSF is determined using isolated stars in the unsubtracted images, and the image subtraction uses a pixelized kernel (similar to that in Bramich 2008). The SN position is measured from epochs when the SN is present with the highest S/N (typically the position is determined to better than 0.05–0.1 pixels), and then the PSF photometry is performed in all images with this position fixed, avoiding biases in the low-S/N regime (see appendix B of Guy et al. 2007 for a discussion).

The flux calibration is to the SDSS (York et al. 2000) Data Release 10 (Ahn et al. 2014) if the SN lies within that survey's footprint, or otherwise to the photometric catalogue of Ofek et al. (2012b) for R_{P48}, or the AAVSO Photometric All-Sky Survey (APASS; Henden et al. 2009), for the other filters.

Our method is sensitive to variation in the data at very early times, i.e. very low flux levels, it is important to test for systematic effects. This was performed by averaging the points before the SN first light. Prior to the explosion, the flux level is consistent with 0, with no evidence of a systematic offset, as shown in Fig. 1.

An example of the data used can be found in Table 2, and the entire data set is available in online supplemental material.

We determine the light-curve parameters for each SN Ia in our sample using the SIFTO light-curve fitter (Conley et al. 2008). SIFTO manipulates the properties of a time series SN Ia spectral energy distribution (SED) in order to best fit an observed light curve, returning the SN stretch (s), the time of maximum light in the rest-frame B band (t_{max}), a peak magnitude, and a colour parameter c for SNe with data in more than one observed filter. We then define all phases (τ) in the SN light curve as relative to this maximum light, i.e. $\tau = t - t_{max}$, thus epochs prior to maximum light have negative phases.
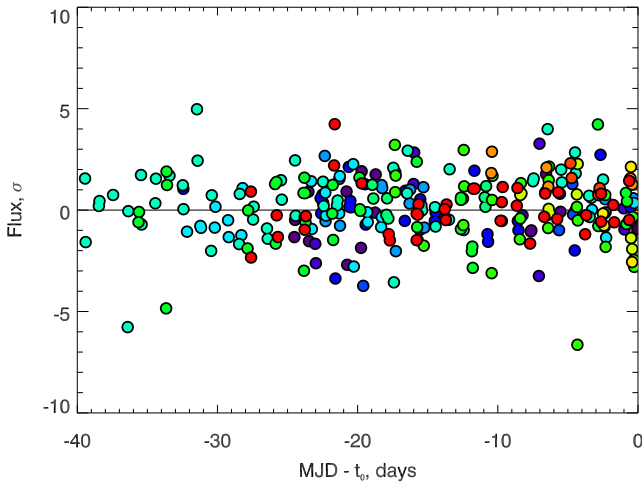
Figure 1. Flux prior to first light for our entire sample. No evidence of a systematic offset is found. Each colour represents a different SN in our sample (online version only).

We note that the use of SIFTO rather than (e.g.) SALT2 (Guy et al. 2007) is not critical in this paper as we do not make use of the peak magnitudes of the SNe, nor their Hubble residuals. The SIFTO stretch and SALT2 equivalent (x_1) agree very well for the same objects (e.g. Guy et al. 2010).

The spectral time series template used by SIFTO assumes a t^2 photometric evolution in the B band at phases $\tau \leq -10$ (equivalently 8–10 d post-explosion for a normal SN Ia) due to a lack of accurate early SN Ia photometric data at the time the SIFTO package was written. Since in this paper we are primarily interested in the behaviour of this early time data, we remove all data with $\tau < -10$ when

fitting with SIFTO. We use an iterative fitting process to do this, first using all the data to estimate the $\tau = -10$ epoch, and then refitting with data earlier than this removed.

2.3 Sample selection

As our study requires well-sampled and relatively high-S/N data, there are several selection criteria that we make. We only allow SNe with both more than three epochs of data and more than four photometric points within the calculated fitting region (Section 3.3, Fig. 5), as fewer would be insufficient to constrain the free parameters in the model. Light curves with more than 4 d between any two consecutive points are also excluded.

The distribution of stretch and redshift for our sample can be seen in Fig. 2. Using a Kolmogorov–Smirnov test, the stretch distribution of our sample is consistent with being drawn from the same distribution as the larger PTF sample with a probability of 91 per cent. Our mean redshift, $z = 0.037$, is slightly lower than that of the parent $z < 0.09$ PTF sample, which has a mean redshift $z = 0.056$.

3 ANALYSIS METHODS

We now turn to the analysis methods we will use in this paper, before presenting the results in Section 4. We begin with a discussion on the parametrization used to fit the early portion of SN Ia light curves.

3.1 Rise-time parametrization

The most widely used model parametrization for the early time SN Ia flux, f_{model}, as a function of time, t, is

$$f_{model}(t) = \alpha(t - t_0)^n, \tag{1}$$

Table 2. Table of example data for one SN, PTF09dsy. Data for the full sample can be found in online supplemental material.

| SN PTF09dsy	MJD	Counts	Δ Counts	Filter	Zero-point	Redshift
	55054.441	−67.7	98.2	R_{P48}	27.000	0.0131 ± 0.001
	55054.460	−68.7	72.3	R_{P48}	27.000	0.0131 ± 0.001
	55055.460	480.0	101.0	R_{P48}	27.000	0.0131 ± 0.001
	55055.472	457.2	67.6	R_{P48}	27.000	0.0131 ± 0.001
	55059.443	8599.9	93.5	R_{P48}	27.000	0.0131 ± 0.001
	55059.463	8603.4	94.4	R_{P48}	27.000	0.0131 ± 0.001
	55061.434	16 360.3	142.9	R_{P48}	27.000	0.0131 ± 0.001
	55061.459	16 634.9	104.1	R_{P48}	27.000	0.0131 ± 0.001
	55063.438	27 290.6	123.8	R_{P48}	27.000	0.0131 ± 0.001
	55063.483	26 937.5	143.1	R_{P48}	27.000	0.0131 ± 0.001
	55066.421	38 663.8	301.7	R_{P48}	27.000	0.0131 ± 0.001
	55066.466	39 415.6	192.0	R_{P48}	27.000	0.0131 ± 0.001
	55069.410	46 253.4	201.1	R_{P48}	27.000	0.0131 ± 0.001
	55069.455	46 201.3	209.2	R_{P48}	27.000	0.0131 ± 0.001
	55080.373	30 495.7	222.8	R_{P48}	27.000	0.0131 ± 0.001
	55080.461	29 730.6	248.6	R_{P48}	27.000	0.0131 ± 0.001
	55087.350	24 598.7	169.6	R_{P48}	27.000	0.0131 ± 0.001
	55087.395	24 978.9	178.0	R_{P48}	27.000	0.0131 ± 0.001
	55089.381	23 637.7	162.0	R_{P48}	27.000	0.0131 ± 0.001
	55089.425	23 756.2	197.7	R_{P48}	27.000	0.0131 ± 0.001
	55093.351	20 758.2	147.4	R_{P48}	27.000	0.0131 ± 0.001
	55093.395	20 267.0	159.0	R_{P48}	27.000	0.0131 ± 0.001
	55095.338	18 196.5	117.7	R_{P48}	27.000	0.0131 ± 0.001
	55095.382	18 400.1	168.8	R_{P48}	27.000	0.0131 ± 0.001
	55107.311	8207.5	146.7	R_{P48}	27.000	0.0131 ± 0.001
	55107.355	8001.8	136.7	R_{P48}	27.000	0.0131 ± 0.001
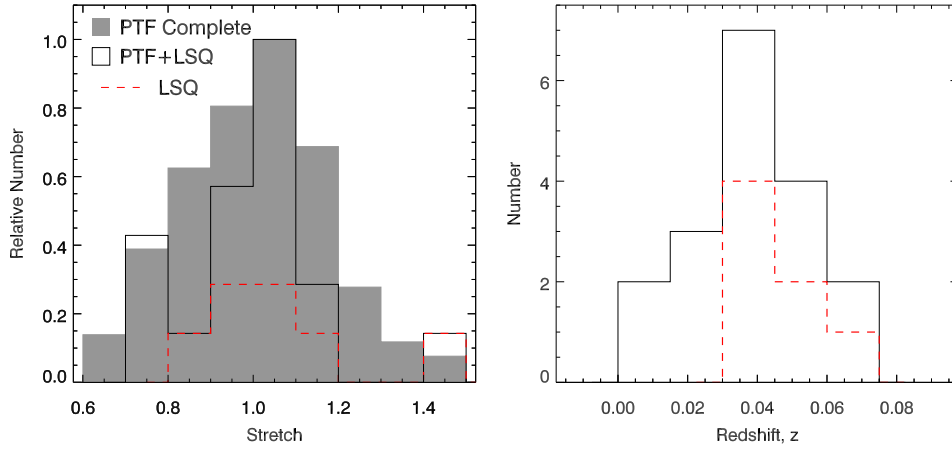
Figure 2. Left-hand panel: the stretch distribution of our combined PTF and LSQ (black) and LSQ (red) data sets. The stretch was measured using SIFTO on data later than $\tau < -10$, as detailed in Section 4.1. The grey histogram shows the distribution of the full $z < 0.09$ PTF sample from Pan et al. (2014). Right-hand panel: the redshift distribution of our combined sample.

for $t > t_0$, and 0 otherwise. Here, α is a normalizing coefficient, and t_0 is usually treated as the time of explosion. However, in this work we consider the possibility that the time of the first photons escaping the ejecta, and the actual explosion of the SN, are distinct, and therefore we refer to t_0 as the time of first light. Note that t_0 corresponds to the time at which the first photons leave the ejecta, which may differ from the time at which these photons can be detected by a given instrument. We do not require that the join of this model at early times to the remainder of the SN light curve be continuous.

In the cases of SN 2011fe (Mazzali et al. 2014) and SN 2010jn (Hachinger et al. 2013), the precise measurement of the rise time led to some tension with spectral models, as the t_0 needed to match the observed abundances and spectral velocities is earlier than that derived from the photometry. This implies that either the models are incomplete in some way, or that there is a dark period between the time of the explosion and the emergence of the first photons from the ejecta. This is represented in Fig. 5, by the gap between $(t_{\rm ex}, F)$ and (t_0, F).

Finally, n is the index of the power law. The specific case of $n = 2$ (giving a t^2 dependence) is known as the 'expanding fireball' model, and is used extensively in the literature as a reference model (e.g. Riess et al. 1999; Conley et al. 2006; Strovink 2007; Hayden et al. 2010a; Ganeshalingam et al. 2011; González-Gaitán et al. 2012), as it provides a good empirical match to early time SN Ia observations.

α is often ignored as a nuisance normalization parameter, but physically contains information about the mass, radius, ^{56}Ni, and opacity of the ejecta. Pinto & Eastman (2000a) show that the (bolometric) rise time ($t_{\rm rise}$) depends on the same parameters as α, whilst n is most sensitive to the mass and distribution of ^{56}Ni and the shock velocity (Piro & Nakar 2013). As α and n depend on some of the same underlying physical parameters and processes, degeneracies between them are expected.

The simple fireball model can be justified under the assumption of constant photospheric temperature (T) and ejecta velocity (v) (Riess et al. 1999). Assuming that the emitting region is hot enough and the SN is approximately represented by a blackbody, the standard optical passbands lie in the Rayleigh–Jeans tail of the SN SED and the SN flux will be $f \propto r^2 T \propto v^2 (t - t_{\rm ex})^2 T$, which for constant v and T leaves $f \propto (t - t_{\rm ex})^2$. It should be noted that if T is constant, then the bolometric luminosity rises quadratically as well. An assumption of a t^2 rise was also shown by Arnett (1982) to be rea-

sonable, as the heating by radioactive decay should approximately balance any adiabatic losses.

These underlying assumptions are, however, unrealistic over time-scales greater than a few hours. A more sophisticated treatment, following Arnett (1982), is presented in the analysis of SN 2011fe in Nugent et al. (2011), who show that the t^2 relation is expected without relying on the same assumptions. The rate of change of the internal energy can be defined as a relationship between the energy deposited by ^{56}Ni, the radiated luminosity and the internal radiation pressure. Their method assumes that radiation pressure dominates and that the energy from ^{56}Ni is thermalized throughout the ejecta. Their final, crucial assumption is that the elapsed time is much less than the ^{56}Ni decay time, $t_{56} = 8.8$ d. Despite the excellent fit to the data ($g_{\rm P48}$, in this case of SN 2011fe), Nugent et al. (2011) concede that this treatment is itself probably simplistic in its analysis of the diffusion wave and distribution of ^{56}Ni. If there is any colour evolution, then the bolometric light curve will not be well fit by the same parameters.

This is developed further by Piro (2012) who predict that the fireball model value of $n = 2$ should be multiplied by a coefficient related to the ^{56}Ni density gradient through the ejecta and the shock velocity. This means that a single value of n for all SNe Ia is not expected, and a range of n is predicted instead.

Another method to probe both the structure of the ejecta and the assumptions is to investigate how the fit deviates from a $n = 2$ fireball model over time. The assumptions made in deriving the fireball model (outlined in Nugent et al. 2011) are strongest soon after explosion and weaken at later times. As a result, in later sections, we consider a modified fireball model

$$f_{\rm model}(t) = \alpha(t - t_0)^{n_0 + \dot{n}(t - t0)}, \tag{2}$$

where n_0 is the rise index at time t_0 and $\dot{n}$ is a variable measuring the deviation from the fireball model as time progresses.

3.1.1 Alternative parametrization

A more recent parametrization for the early light curve uses a broken power law (Zheng et al. 2013):

$$f_{\rm model}(t) = \beta \left(\frac{t - t_0}{t_{\rm b}} \right)^{\alpha_1} \left[1 + \left(\frac{t - t_0}{t_{\rm b}} \right)^{s(n_1 - n_2)} \right]^{-1/s}, \tag{3}$$

where β is a normalization constant, t_0 is the time of first light, t_b is the break time, n_1 and n_2 are the two rise indices before and after the break, and s is a smoothing parameter. The motivation behind this approach is that changes in the index of a power law are a result of drastic changes in the temperature and velocity of the fireball at very early times; the opposite of the assumptions in the fireball model. An additional contribution may come from the shock-heated cooling emission from the initial shock breakout. To date, two SNe have been fitted with this model: SN 2013dy (Zheng et al. 2013) and SN 2014J (Goobar et al. 2014; Zheng et al. 2014), in both cases predicting a faster rise time than that from a single power-law model.

3.2 Fitting methods

We perform fits of equation (1) to our data, correcting for $1 + z$ time dilation, using a grid-search minimization of the χ^2 statistic over our three free parameters; α, t_0 and n, i.e.

$$\chi^2 = \sum \left(\frac{F - f_{\mathrm{model}}}{\sigma_F} \right)^2 \tag{4}$$

where F and σ_F are the SN flux measurements and uncertainties, f_{model} is the model SN flux from equation (1), and the sum runs over all the data points. We compute probabilities over a grid and report the mean value of the marginalized parameters as the best fits, with our quoted uncertainties enclosing 68.3 per cent of the probability. The conversion from χ^2 to probability, P, is $P \propto e^{-\frac{\chi^2}{2}}$.

The grid size is chosen to enclose as close to 100 per cent of the probability as is measurable. Specifically, we chose ranges of: $-15 < t_0 - t_0(n = 2) < 10$, where $0.0 < n < 8.0$ and $-9 < \log(\alpha) < 0$. An example of the range covered, and probability distribution, can be seen in Fig. 3. We sample $\log(\alpha)$ rather than α to better sample low values of α, while maintaining dynamic range.

This is a different, and slightly more direct approach to that used in Conley et al. (2006) and Ganeshalingham et al. (2011), in which Monte Carlo simulations are used to estimate the parameter uncertainties. However, those analyses were performed on stacked light-curve data (rather than fitting individual objects), which require a careful correction of the light-curve shape and SN flux normalization. This can introduce covariances between stacked data points,
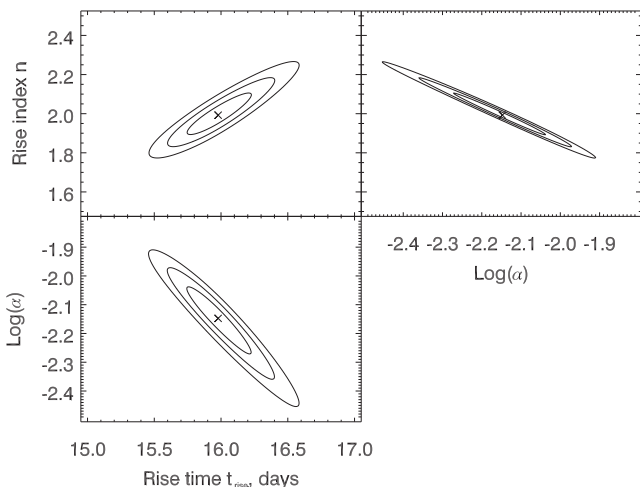
which demands a more sophisticated Monte Carlo like approach to handle these covariances.

The ellipticity of the contours in Fig. 3 demonstrate the covariance between the parameters in a typical fit. The strongest is found between n and $\log(\alpha)$ but is present in significant strength between all of the variables.

3.3 Defining the rise-time region

The simple rise-time model of equation (1) will only hold over the first few days of the SN evolution, as at some epoch the rise of the SN slows and eventually reaches a maximum point. Thus, our first task is to determine over which range the model holds, and thus over which range we can fit data.

Both Conley et al. (2006) and Ganeshalingam et al. (2011) define the rise-time region as earlier than 10 d before B-band maximum light, (i.e. $\tau < -10$). This may occur at a different number of days post-explosion for different SNe Ia due to the stretching of the SN light curves. As we are not stretch-correcting the raw data in this study, prior to fitting, we instead prefer a definition relative to t_0.

We first fit the fireball model with an initial rise-time region of $\tau < -10$. This gives a first estimate of t_0 with $n = 2$. We then re-fit the light curve using data ranging from 2 to 18 d after t_0, and record the values of n and t_{rise}, and the χ^2 (Fig. 4). The discontinuous jumps in Fig. 4 are due to the inclusion of more data as the epoch range expands.

The choice of the fitting region must balance two competing constraints: there must be sufficient data to allow a meaningful rise-time fit, yet the fitting region must not reach too far into the photometric evolution where the rise-time parametrization does not hold. Balancing these requirements across the sample, as well as taking into account the stability of the result is challenging.

In many cases, the cut-off time that best satisfied these constraints was nearly coincident with $t_{0.5}$, the time at which the SIFTO light curve was at half of its maximum value (see Fig. 5). $t_{0.5}$ is not reliant on either the stretch or a fixed number of days, so is an ideal choice as a limit of the fitting region. It is also broadly consistent with $\tau < -10$ if the light curve was stretch-corrected. To ensure a consistent definition of $t_{0.5}$, after fitting, the value of $t_{0.5}$ is re-calculated using the best fit to the data. This is in most cases almost indistinguishable from that calculated from SIFTO, indicating a good match, but is free of any reliance on the later time data. Fig. 6 shows the outcome of this process, a best fit to PTF 11hub.

This approach is similar to that used in González-Gaitán et al. (2012), where they define their limiting epoch as the 'transition phase', τ_t, where the light curve transitions from the rise to the main body, and they find $-10 \lesssim \tau_t \lesssim -8$.

Following this procedure to define our cut off, our final fit for each SN was performed on the data where $t_0(n = 2) - 2 < t < t_{0.5}$ was satisfied; that is, we fit data up to 2 d before the time of first light, as calculated from an enforced fireball $n = 2$ fit, and less than half of the maximum brightness. Imposing the lower limit was found not to affect the outcome of the fits, but removed contamination of the probability distribution from non-detections.

3.4 Fits to bolometric versus filtered data

Our next task is to establish the validity of comparing fits obtained in different filters and at different redshifts, both for comparison to earlier work, and for comparison between the different surveys in our sample. Ideally, we would measure the rise time on the bolometric output of the SN, but such data are not available, and
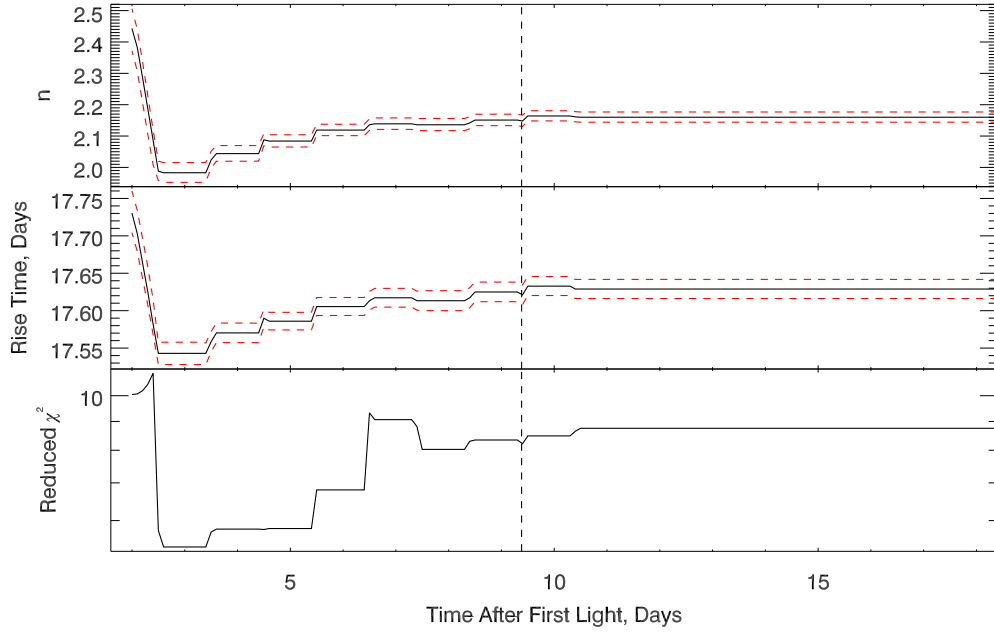

Figure 3. Probability distribution contours from the fit of SN PTF09dsy. Contours enclose 99.73, 95.45, and 68.37 per cent of the total probability.

Figure 4. The fit parameters for SN 2011fe as a function of the epoch range over which the fit is performed, from 2 to 18 d after first light. Top panel: the change in n. Middle panel: the variation in rise time. Bottom panel: the evolution of the goodness of fit statistic, χ^2 per degree of freedom, as defined in equation (4). The vertical dashed line shows the time at which the light curve reaches half of its maximum value ($t_{0.5}$).
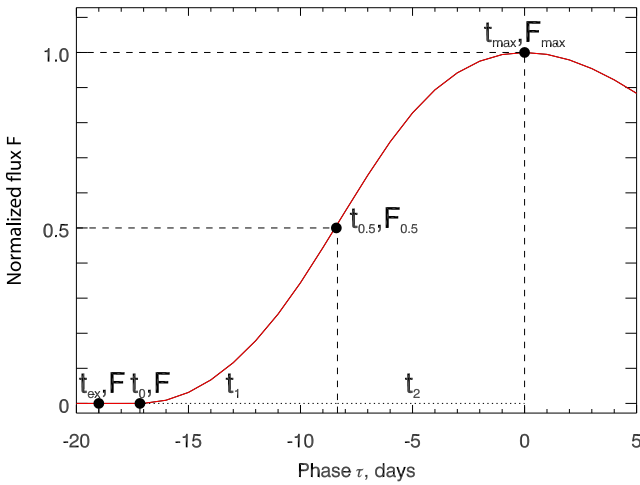

Figure 5. Schematic diagram of an SN Ia light curve. The so-called dark phase occurs between the time of explosion, t_{ex} and the time of first light, t_0. Also shown is the rise time split into its two sections: t_1 is the region within which our fitting is performed, t_2 is the time from the end of the fitting region up to maximum light.

Figure 6. An example SN Ia light curve, best-fitting model, and residual, for SN PTF11hub. The fit parameters can be found in Table 4. Uncertainties are plotted but are small, residual is shown for clarity.

hence we need to examine any biases that might result; essentially, we are testing the effect of *k*-corrections. We test this by using the very well observed nearby SN Ia SN 2011fe, which has significant spectroscopic and photometric early time data.

We use 15 available pre-maximum spectra from the literature of SN 2011fe (Nugent et al. 2011; Parent et al. 2012; Pereira et al. 2013; Mazzali et al. 2014). We measure synthetic light curves from

these spectra in the *B*, *V*, g_{P48}, R_{P48}, and gr_{LSQ} filters, as well as a 'pseudo-bolometric' band with a wavelength range 3500–9000 Å, with each spectrum scaled so that its synthetic g_{P48} magnitude matched that measured from the real g_{P48} photometry. Using the

Table 3. Results for the SN 2011fe synthetic light curves. Δn is the difference between n in a given filter and that of the pseudo-bolometric, i.e. $n^{\text{filter}} - n^{\text{Pseudo-bol}}$. Similarly, Δt is the difference between t_{rise} in a given filter and pseudo-bolometric, i.e. $t_{\text{rise}}^{\text{filter}} - t_{\text{rise}}^{\text{Pseudo-bol}}$ nResults in g_{P48} differ from Nugent et al. (2011) as a result of fitting a longer segment of the light curve.

Filter	n	Δn	t_{rise}, (d)	Δt_{rise} (d)
Pseudo-bol	2.23	0.0	17.75	0.0
B	2.05	-0.18	17.13	-0.62
V	2.33	0.1	18.54	0.79
g_{P48}	2.15	-0.08	17.62	-0.13
R_{P48}	2.15	-0.08	18.14	0.39
gr_{LSQ}	2.20	-0.03	17.94	0.19

spectral templates of Hsiao et al. (2007), this pseudo-bolometric filter contains $\simeq 70$ per cent of the bolometric flux at $t_{0.5}$ (corresponding to $\tau = -8.9$), and $\simeq 72$ per cent of the flux at maximum light. The wavelength range of the pseudo-bolometric filter was chosen as it is covered by most of our available spectra.

The uncertainties in our synthetic light curves come from the g_{P48} photometric uncertainties, with an additional systematic uncertainty added in quadrature arising from relative flux calibration errors (e.g. differential slit losses). We estimate this to be 1 per cent. These synthetic light curves were then fitted as described in Section 3.2, and the results are in Table 3.

3.4.1 The effect of different filters

The results show some differences between different filters, due to rapid evolution in the spectral features in each band. Fig. 7 shows how the flux in each filter, relative to pseudo-bolometric flux at that epoch, changes with time. The g_{P48} band shows an almost constant flux ratio, but R_{P48} decreases with time, while the B-band increases. The pseudo-bolometric value, 2.23 is greater than that in

g_{P48}, and greater than 2, in agreement with the findings of Piro & Nakar (2014). The broadest filter, gr_{LSQ}, is obviously the closest to bolometric, but also shows a decreasing flux ratio. Note that earlier work has predominantly used data either in, or corrected to, the B band. Table 3 shows that this fit has an n closest to 2; however, it is significantly lower than the values in the other filters, and is not consistent with the pseudo-bolometric value.

In an attempt to further understand the colour evolution and its effect on n, templates from SALT2 (Guy et al. 2007) and Hsiao et al. (2007)/SIFTO (Conley et al. 2008) were analysed, however, the nature of the investigation probes the very earliest epochs, where there have been few spectral observations. For example, the earliest Hsiao et al. (2007) templates pre-maximum are based on six spectra with an average epoch of $\tau = -11.6$ d. Because of this, and despite being a single example, the data from SN 2011fe are the best resource available at very early times. Comparing with SN 2013dy (Zheng et al. 2013), the colour evolution is similar, although SN 2011fe exhibits a stronger Ca II IR triplet compared with SN 2013dy within the first 2 d. This does not fall within any of our filters, but falls within the pseudo-bolometric range.

In summary, by considering the different fits to our simulated photometry, we estimate the systematic effect of using different filters to be $n \pm 0.1$.

3.4.2 The effect of redshift

As our sample lies across a range of redshifts, we also need to ascertain the impact that this has on the colour evolution. To do this, we performed the same procedure as in Section 3.4.1, redshifting the spectra each time, up to our maximum redshift of $z = 0.07$ before fitting. The results of these tests can be seen in the right-hand panel of Fig. 7.

We find that the broad gr_{LSQ} filter provides data that are very stable with redshift, the value of n remaining almost static. Leaving the rest frame, the measured n in R_{P48} and g_{P48} diverges, with the R_{P48} increasing and the g_{P48} decreasing more steadily. The scatter around
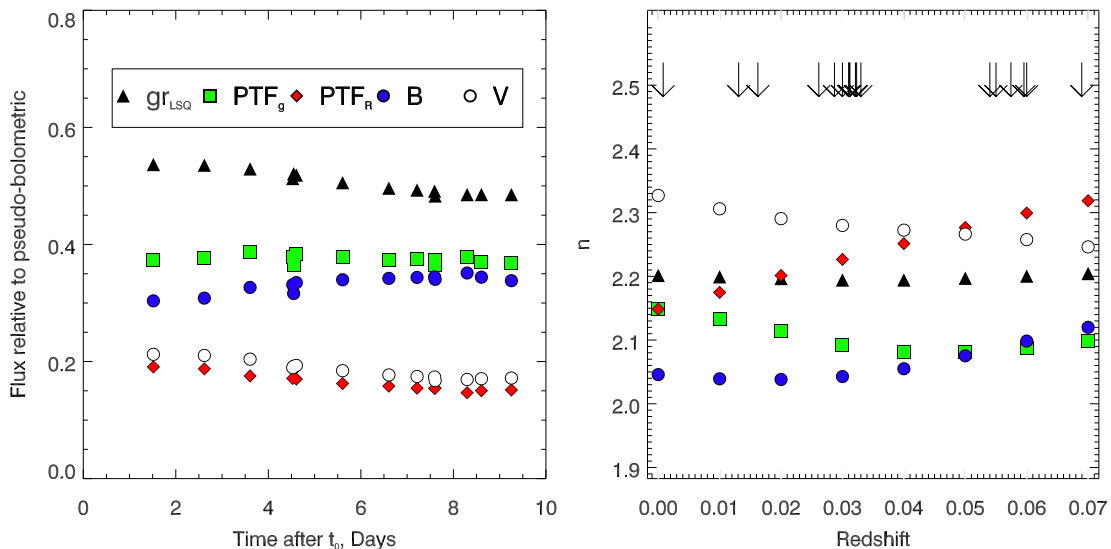

Figure 7. Left-hand panel: the flux of SN 2011fe through various filters relative to a pseudo-bolometric flux (see Section 3.4 for details) as a function of epoch. The filters are (top to bottom) gr_{LSQ}, g_{P48}, B, V, and R_{P48} filters. Right-hand panel: the fits to the redshifted spectra of SN2011fe, over the range of redshifts covered by our sample. The scatter around the mean redshift is consistent with the values found in the neighbouring panel. The arrows at the top of the figure show where our SNe lie.

the mean redshift ($z = 0.036$) is consistent with the dispersion between filters in Table 3.

In summary, we estimate the systematic effect of redshift to be reflective of that from using different filters, since the low redshifts do not shift the spectra by more than the width of our filters, that is, a systematic effect of at most $n \pm 0.1$.

3.4.3 The effect of extinction

We also performed these checks after reddening the spectra by $E(B - V) = 1$ and found no significant deviation in results. Additionally, inspecting the spectra at maximum light of each PTF object in our sample, we find evidence of Na ID absorption in only two SNe (PTF11gdh and PTF12gdq). These are discussed in Section 4 but do not appear to be unusual events.

4 RESULTS

We now present the results of applying our fitting methods (Section 3.2) to our data sample (Section 2.3). We first discuss the rise-time analysis, followed by the rise index. Our results can be found in Table 4.

4.1 The SN Ia rise time

The average rise time of the 18 SNe Ia in our sample with n a free parameter in the fit, is $t_{rise} = 18.98 \pm 0.54$ d, or $t_{rise} = 18.97 \pm 0.44$ d if the rise times are stretch-corrected, where the uncertainties in both cases are the standard error on the mean. (We exclude one SN, PTF12emp, from this latter calculation as there is insufficient data to reliably estimate a stretch.) For the stretch correction, we use SIFTO to measure the stretch based on photometry later than $\tau = -10$, and so it is independent of the shape of the early light curve. These values are longer than those found in previous work. Assuming $n = 2$, the mean rise times are $t_{rise} = 17.86 \pm 0.42$ d uncorrected and $t_{rise} = 17.90 \pm 0.33$ d, after stretch correction. The $n = 2$ rise times are shorter in both cases. These values are consistent with Ganeshalingam et al. (2011), but lower than Conley et al. (2006) and higher than those found in both Hayden et al. (2010a) and González-Gaitán et al. (2012) by 3σ.

The histogram of the rise-time distributions can be found in Fig. 8. Strovink (2007) previously suggested that there may be two rise-time modes, once the rise times have been corrected for the overall shape of the light curve (using the fall time). We do not find any evidence for this using either $n = 2$ or n-free.

Hayden et al. (2010a) and Ganeshalingam et al. (2011) both find that the fraction of their sample that are slowest to decline after peak are amongst the fastest to rise. Both studies therefore parametrize the width of the light curve using two-stretch parameters, one pre- and one post-maximum. Ganeshalingam et al. (2011) also find that the luminous SNe Ia have a faster rise than expected based on a single stretch value. We see a similar trend in Fig. 9, also lower stretch SNe appear to have slower light curves than would be expected from a single stretch.

In Fig. 10, we show the relation between stretch (again calculated without the very early photometric data) and t_{rise}. A correlation is expected and observed in the data. The results are also shown for when $n = 2$ showing, on average, shorter rise times.

The rise time can be decoupled into two components: t_1, the time between first light (t_0) and the time of half-maximum ($t_{0.5}$), and t_2, the time between $t_{0.5}$ and t_{max} (shown in Fig. 5). As can be seen in Fig. 11, surprisingly, these two time-scales do not show a particularly strong dependence, having a Pearsons Correlation Coefficient $P = 0.61$, and when imposing a stretch cut commonly used in cosmology, $0.7 \leq s \leq 1.3$ (Conley et al. 2011), which excludes LSQ12gpw, this drops to 0.43. As the SIFTO fit includes data from $\tau > 10$, which is roughly consistent with $t_{0.5}$, it is unsurprising

Table 4. Table of results.

| SN	t_{max}, MJD	t_{rise}, (d)	n	$\dot{n}$	Stretch	χ^2_{DOF}	RA (J2000)	Dec. (J2000)	Filter
PTF09dsy	55070.4 ± 0.1	15.98 ± 0.20	$2.00^{+0.08}_{-0.07}$	$0.0^{+0.13}_{-0.01}$	0.80 ± 0.01	0.58	3:33:22.1	$-04:59:55.2$	PTF48R
PTF10accd	55556.0 ± 0.2	$18.17^{+0.46}_{-0.32}$	$1.48^{+0.19}_{-0.12}$	-0.02 ± 0.01	1.11 ± 0.02	0.78	02:13:30.4	46:41:37.2	PTF48R
PTF10duz	55285.0 ± 0.2	$17.5^{+3.7}_{-1.0}$	$1.96^{+1.5}_{-0.46}$	$-0.005^{+0.02}_{+0.01}$	1.00 ± 0.03	1.88	12:51:39.5	14:26:18.7	PTF48R
PTF10hml	55352.3 ± 0.1	$19.4^{+2.7}_{-1.5}$	$2.31^{+1.08}_{-0.53}$	$0.01^{+0.01}_{-0.02}$	1.07 ± 0.02	1.50	13:19:49.7	41:59:1.6	PTF48R
PTF10iyc	55361.5 ± 0.1	$19.4^{+4.4}_{-1.4}$	$2.08^{+2.00}_{-0.70}$	$0.00^{+0.02}_{-0.03}$	1.10 ± 0.02	1.04	17:09:21.8	44:23:35.9	PTF48R
PTF11gdh	55744.1 ± 0.1	19.57 ± 1.8	$2.26^{+0.58}_{-0.55}$	-0.005 ± 0.01	1.07 ± 0.03	1.25	13:00:38.1	28:03:24.1	PTF48R
PTF11hub	55770.0 ± 0.2	$16.50^{+0.96}_{-0.76}$	$2.17^{+0.35}_{-0.26}$	0.005 ± 0.01	0.80 ± 0.01	1.17	13:12:59.5	47:27:40.3	PTF48R
PTF11kly/SN2011fe	55814.3 ± 0.1	17.59 ± 0.1	2.15 ± 0.02	0.011 ± 0.001	0.965 ± 0.009	8.06	14:30:5.8	54:16:25.2	PTF48g
PTF11qnr	55902.3 ± 0.1	$17.01^{+1.0}_{-0.7}$	$2.99^{+0.49}_{-0.32}$	$0.025^{+0.01}_{-0.005}$	0.79 ± 0.04	1.57	22:44:25.4	$-00:10:2.0$	PTF48R
PTF12emp	56080.9 ± 0.4	$19.9^{+1.9}_{-1.0}$	$2.36^{+0.76}_{-0.37}$	$0.01^{+0.01}_{-0.01}$	1.13 ± 0.14	3.52	13:13:53.7	34:06:59.7	PTF48R
LSQ12fxd	56246.4 ± 0.1	$23.8^{+1.8}_{-1.3}$	$3.24^{+0.53}_{-0.36}$	$0.02^{+0.02}_{-0.2}$	1.17 ± 0.01	2.77	05:22:17.0	$-25:35:47.0$	LSQgr
PTF12gdq	56116.3 ± 1.8	$17.6^{+4.7}_{-2.3}$	$2.34^{+1.86}_{-0.61}$	0.015 ± 0.02	0.94 ± 0.02	2.06	15:11:35.3	09:42:34.0	PTF48R
LSQ12gpw	56268.4 ± 0.1	$24.7^{+3.2}_{-1.6}$	$2.74^{+1.00}_{-0.50}$	0.015 ± 0.01	1.42 ± 0.02	5.79	03:12:58.2	$-11:42:40.0$	LSQgr
LSQ12hxx	56289.8 ± 0.1	$19.9^{+2.3}_{-1.3}$	$3.70^{+1.08}_{-0.61}$	0.04 ± 0.01	1.00 ± 0.03	2.00	03:19:44.2	$-27:00:25.6$	LSQgr
LSQ12hzj	56300.8 ± 0.2	$18.5^{+0.6}_{-0.8}$	$2.61^{+0.37}_{-0.47}$	$0.045^{+0.02}_{-0.03}$	0.97 ± 0.05	20.19	09:59:12.4	$-09:0:8.30$	LSQgr
LSQ13ry	56394.9 ± 0.1	$19.0^{+1.5}_{-0.8}$	$3.03^{+0.64}_{-0.37}$	0.025 ± 0.01	0.86 ± 0.02	1.81	10:32:48.0	04:11:51.4	LSQgr
LSQ13cpk	556590.0 ± 0.1	$17.01^{+0.15}_{-0.25}$	$1.87^{+0.07}_{-0.13}$	$0.02^{+0.04}_{-0.2}$	1.05 ± 0.03	1.77	02:31:3.8	$-20:08:49.6$	LSQgr
LSQ13des	56638.9 ± 0.1	$20.0^{+3.9}_{-2.3}$	$2.64^{+1.37}_{-0.8}$	0.01 ± 0.01	0.96 ± 0.03	2.79	03:25:18.9	$-23:42:3.5$	LSQgr
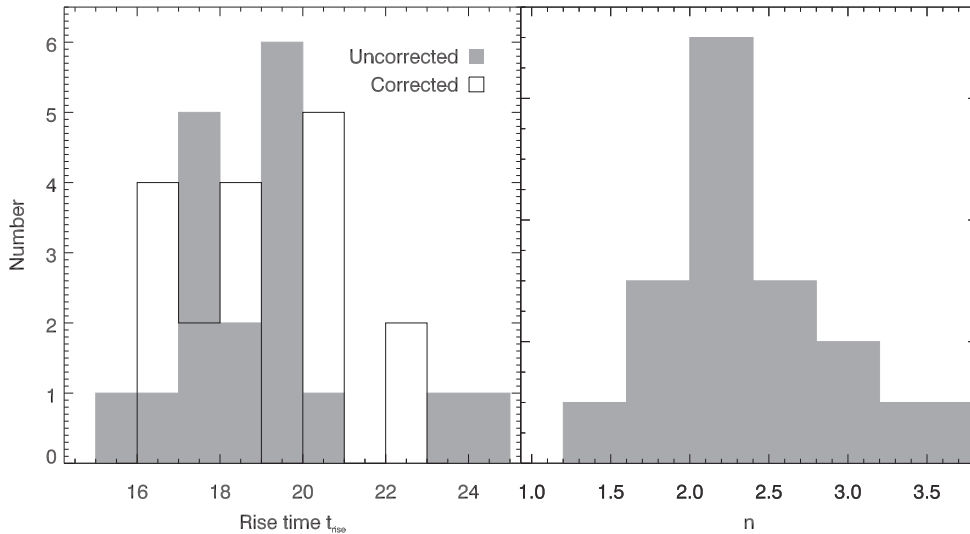
Figure 8. Left-hand panel: histogram showing the distribution of rise times for our sample leaving n as a free parameter. The solid grey histogram shows the raw rise time, while the unshaded histogram shows the rise time corrected for stretch. Right-hand panel: the histogram of the best-fitting rise-index (n) values. The distribution has $n_{mean} = 2.44 \pm 0.13$ and $n_{median} = 2.33$ with a slight positive skew.
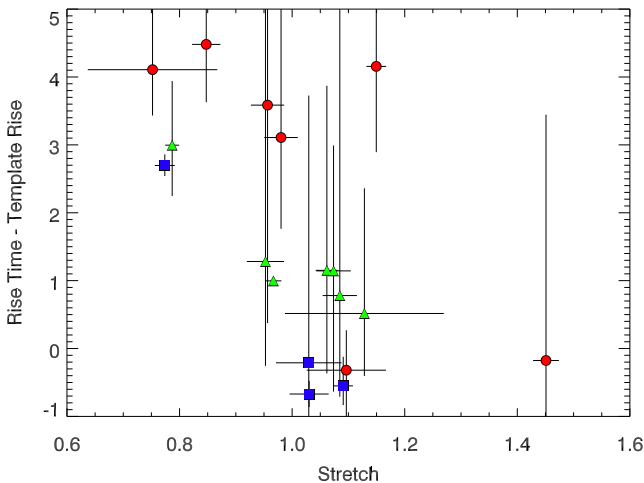

Figure 9. The difference between the measured t_{rise} and the t_{rise} expected from our SN template based on the fit stretch, plotted against the stretch. The coloured points denote a binning by the rise index. Red circles are $n > 2.4$, green triangles $1.9 < n < 2.4$, and blue squares $n < 1.9$. Higher stretch SNe Ia have a t_{rise} that is faster than that implied by the stretch-corrected template t_{rise}.

Figure 10. Stretch versus rise time. The black points are those fitted with a free n parameter, the hollow points are those where the fitting has been constrained to $n = 2$.

that there is a strong correlation between t_2 and stretch (Fig. 12), with $P = 0.89$. However, there is also no strong relationship between stretch and t_1 (Fig. 12) ($P = 0.57$, which weakens to $P = 0.34$ when imposing a stretch cut).

The diversity of the early time light curves in our sample can be seen in Fig. 13. The light curves have been stretch-corrected and normalized, and shifted to have a coincident $t_{0.5}$. Whilst when stretch-corrected, in the t_2 distribution the scatter is reduced, the data in t_1 still show a large amount of variation (Fig. 13). This variation, even after stretch correction, may have been lost within instrumental noise in previous surveys. To avoid introducing additional systematics due to misinterpreting this scatter, care must be taken when using SNe Ia data in this region for cosmology as the variation is significant.

4.2 The rise index – '*n*'

The distribution of the n parameter, which can be seen in Fig. 8, has a mean of $n = 2.44 \pm 0.13$ and a tail in the distribution towards higher n. When corrected to a pseudo-bolometric value, as discussed in Section 3.4, this becomes $n = 2.50 \pm 0.13$. Both mean values, corrected and uncorrected, are not consistent with the $n = 2$ fireball model, although individual SNe Ia within the sample are consistent with $n = 2$ (Table 4); the n values broken by SN name are shown in Fig. 14. To compare with previous work (Table 1), our n value is marginally consistent with Ganeshalingam et al. (2011), who use the low-redshift LOSS sample and find $n = 2.2^{+0.27}_{-0.19}$. Our result is inconsistent with more recent higher redshift studies, Hayden et al. (2010a) or González-Gaitán et al. (2012). Furthermore, the recent study of SN 2014J has yielded a rise index of $n = 2.94 \pm 0.20$ (Zheng et al. 2014). This lends further evidence that there is not only a range of n, but that the centre of the distribution is located
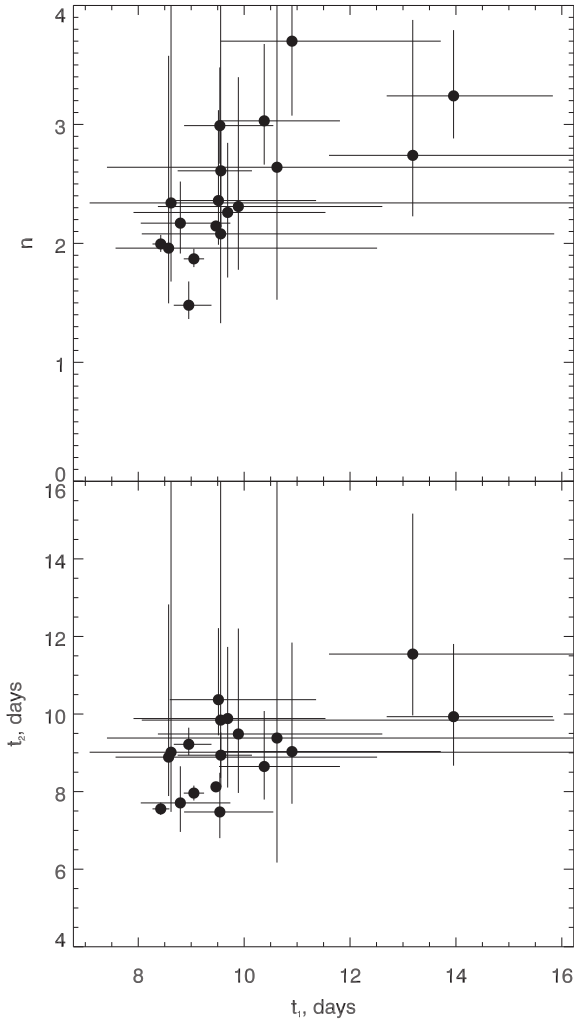
Figure 11. Top panel: n versus t_1, in the region fitted, n correlates with the length of time from t_0 to $t_{0.5}$. Bottom panel: t_2 versus t_1, no strong correlation can be seen between the early t_1 and late t_2 parts of the light curve.
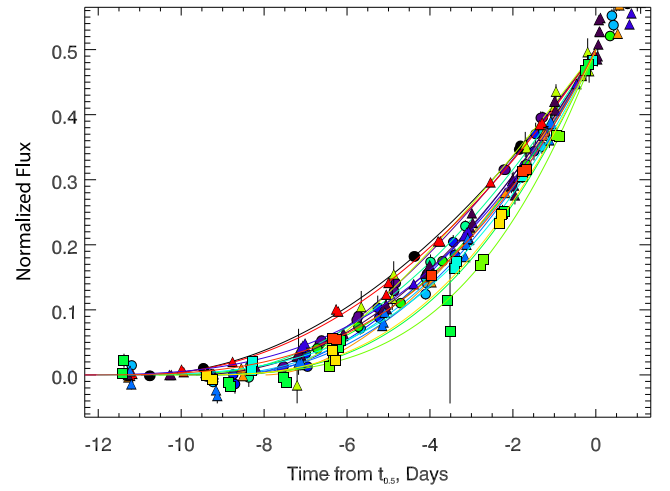

Figure 13. Our sample of 17 SNe Ia (PTF12emp excluded, see Section 4.1), normalized, stretch-corrected and shifted to have coincident $t_{0.5}$. Note the diversity in the early SNe Ia light curves even after stretch correction.

at values $n > 2$. This result supports the finding of Piro & Nakar (2014) that a t^2 rise is not a generic property of SNe Ia.

As mentioned in Section 3.4.3, we see non-zero Na ID absorption lines at the position of the host galaxy in the low-resolution spectra in two SNe: PTF11gdh and PTF12gdq. However, we cannot tell whether this is from the host or from CSM interaction but the measurements of n and $t_{\rm rise}$ are not different from the bulk of the sample. We do not find these SNe to occupy any unusual position in any of the parameter space we investigate. Both have a value of n that is consistent with the mean value within the calculated uncertainties.

We find no evidence of a correlation between n and stretch (Fig. 15, left-hand panel). González-Gaitán et al. (2012) found a weak trend, with larger stretches corresponding with higher n. While both $t_{\rm rise}$ and stretch do not correlate strongly with n, as can be seen in Fig. 15, there is a clear correlation between t_1 and n
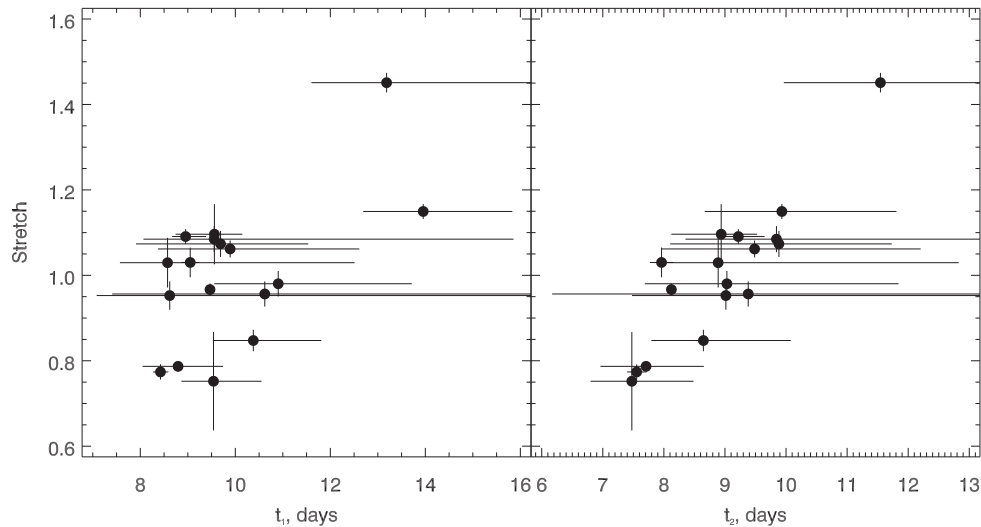
Figure 12. Left-hand panel: stretch versus t_1, no strong correlation can be seen. Right-hand panel: stretch versus t_2, a clear correlation is visible. This is expected as the stretch was measured using data within this region, the strength of the correlation is slightly weaker than expected.
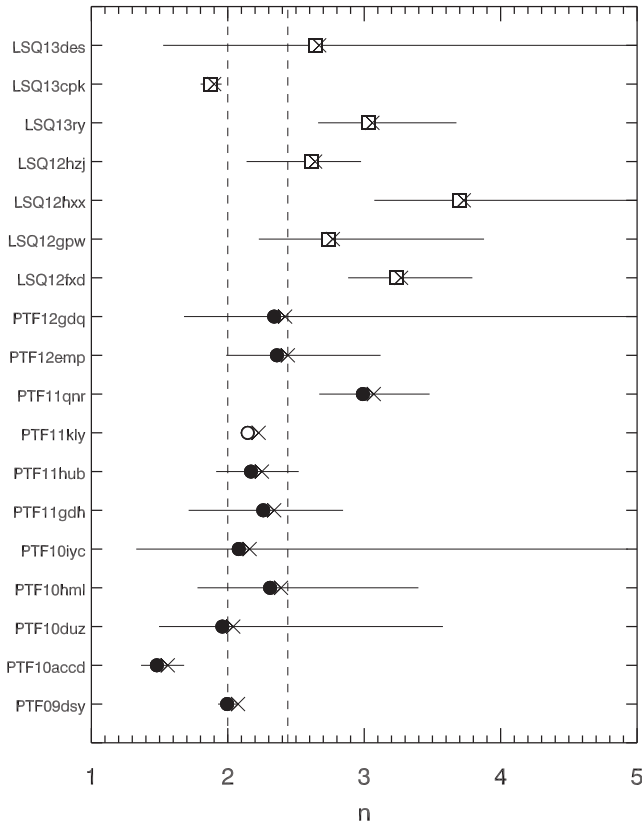
Figure 14. The best-fitting '*n*' and uncertainty for each SN in the sample. The hollow squares are gr_{LSQ} observations, solid circles are R_{P48} and hollow circles are g_{P48}. The dotted lines indicate $n = 2$ and the mean of the sample, $n_{mean} = 2.44 \pm 0.13$. The crosses show the location of the points corrected to the 'bolometric' value of n, if the SN 2011fe correction (Table 3) holds for other SNe.

(Fig. 11, top panel), with the lowest rise indices corresponding to the shortest initial time spans.

A distribution of n values centred above 2 agrees well with previous work on individually fitted SNe (Nugent et al. 2011; Hachinger et al. 2013; Zheng et al. 2013, 2014). However, these fits were done

on rise-time regions of varying sizes, it is for this reason that our value of n for SN 2011fe differs from that of Nugent et al. (2011); in Fig. 4, when the data range fitted is the same, the values are fully consistent. Thus, direct comparisons between studies are difficult, as a shorter, earlier fitting region probes a shallower ejecta region, raising the prospect of a time-dependent index.

4.2.1 A time-dependent index – '$\dot{n}$'

Fig. 4 shows that the n measured changes over time, as more data are added the behaviour of n in Fig. 4, is evidence that this is occurring. This effect explains the difference in n measured in this work ($n = 2.15 \pm 0.02$, for $t_0 \leq t \leq t_{0.5}$) and Nugent et al. (2011) (2.01 ± 0.01 for $t_0 \leq t \leq t_0 + 3$) procedure as outlined in Section 3.2, substituting equation (2) for equation (1).

We find evidence for a positive $\dot{n}$ in most SNe in our sample, with a mean value of $\dot{n} = 0.011 \pm 0.004 \, \mathrm{d}^{-1}$ (where the uncertainty is the standard error on the mean) and a weighted mean value of $\dot{n} = 0.011 \pm 0.001 \, \mathrm{d}^{-1}$. Specifically, in the case of SN 2011fe with n as a free parameter we find $n_0 = 2.02 \pm 0.02$, consistent with Nugent et al. (2011), and an $\dot{n} = 0.011 \pm 0.001 \, \mathrm{d}^{-1}$. This positive $\dot{n}$ (in both cases) reflects that fitting equation (1) we find the mean n greater than 2. We find some evidence that the SNe that have observations longest after explosion are those which, in general, have the largest $\dot{n}$; that is, the largest rate of deviation away from the fireball model. This may be driven physically by the later time data being driven by deeper ejecta layers.

This time dependence of n can also be seen in Fig. 16. When the first observation of an SN is made earlier, the n is lower, due to the different ejecta conditions. Applying a linear fit, an intercept of $n = 1.8 \pm 0.2$ is found, and a slope of $m = 0.39 \pm 0.15$, making the trend significant to 2.6σ. When the observations begin at a later epoch, there is a smaller contribution from the ^{56}Ni in the upper most layers, changing the measured n.

4.2.2 Broken power law

We also performed a fit to SN 2011fe using equation (3). Unlike Zheng et al. (2013) and Zheng et al. (2014) we find no evidence
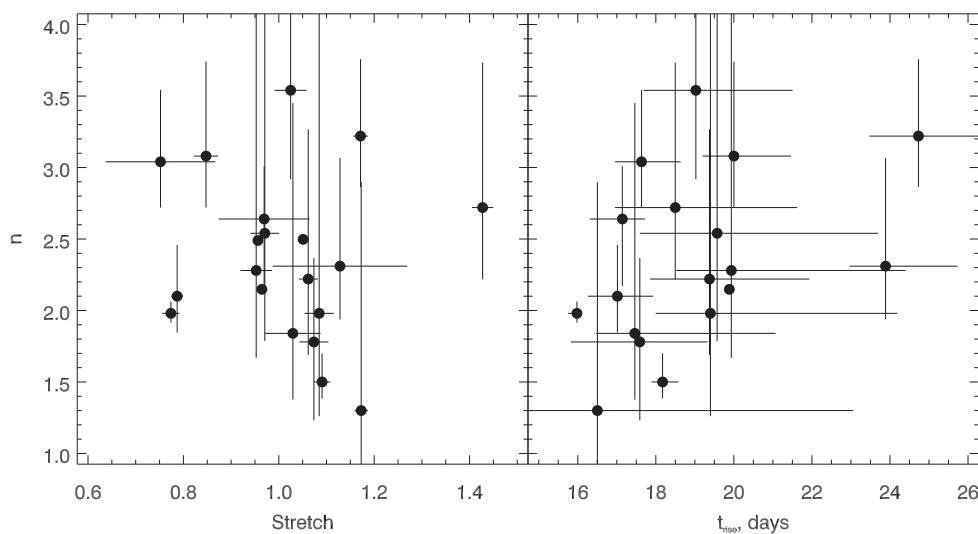

Figure 15. Left-hand panel: n versus stretch for our sample, no evidence of a correlation is found. Right-hand panel: n and t_{rise} do show some evidence of a relationship, but with low significance.
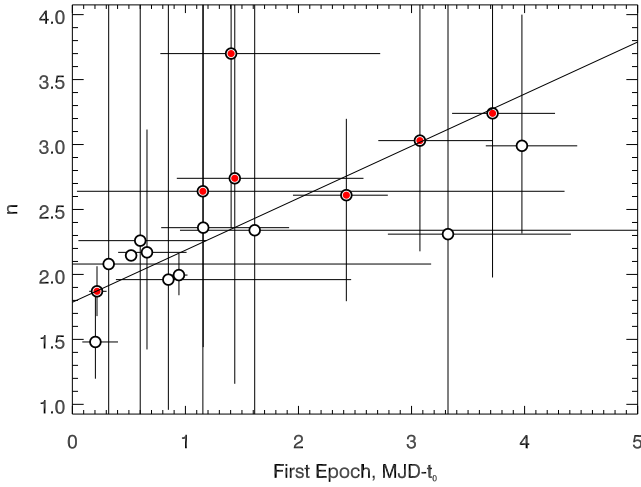
Figure 16. The fitted n plotted against the time of the first observation, relative to t_0 corrected for redshift. LSQ SNe are shown in red (filled) and PTF are shown in white (hollow). The best fit to the data is overplotted.

for a break in the light curve. The data from SN 2011fe contains six data points within the first 3 d after the explosion (i.e. before a 'break time'; $t_b^{2013dy} = 3.14 \pm 0.30$ d and $t_b^{2014J} = 2.61 \pm 0.20$ d), however these are clustered in three epochs, and it may be that subday cadence is needed in this early time to be sensitive to broken power laws.

5 DISCUSSION

In Piro (2012), the first 4 d of data from SN 2011fe were analysed and the implications of a power-law dependence explored, considering the dynamics and thermodynamics of the expanding ejecta in shells. At early times, the emitted luminosity originates from a shell between $\simeq 0.01$ and $0.3\,M_\odot$. Piro (2012) calculate that the power-law scaling for the bolometric luminosity goes as $L(t) \propto t^{2(1 + 1/\gamma + \chi)/(1 + 1/\gamma + \beta)}$ for $t \lesssim t_{56}$, with the polytropic index, $\gamma = 3/2$ for non-relativistic electrons ($\gamma = 3$ for relativistic electrons), and for a radiation pressure dominated shock, $\beta = 0.19$ which controls the rate of change of the shock velocity, while χ characterizes the ^{56}Ni distribution in the ejecta shell. To change the n value, either χ or β must change. Simplifying the expression by setting $\chi = 0$ results in $n \simeq 1.8$. This value is consistent with Conley et al. (2006), despite the fitting region being twice the size of the 4 d for SN 2011fe. If we treat the region from t_0 to $t_{0.5}$ as one shell, as in this parametrization, increasing n is possible by increasing χ, and having deeper ^{56}Ni dominating the rise. However, smaller n are more problematic to explain.

It should be noted that, in Fig. 16, the intercept of the best fit, at $n = 1.8$, is consistent with the above case from Piro (2012). This value is in tension with the findings of higher n values in SN 2013dy and SN 2014J and the justification that the value of n found was due to the unprecedented early discovery and followup. Clearly, data on further SNe collected very soon after first light are needed.

Only one of the SNe in our sample has $n < 1.8$, PTF10accd, and the small uncertainties make it inconsistent with both $n = 2$ and the lower limit of Piro (2012) ($n = 1.8$). It should be reiterated that the bolometric value is expected to be larger than the values in R_{P48} or g_{P48}; however, from our tests in Section 3.4 this would not make PTF10accd consistent with $n = 1.8$.

This result has two possible implications depending on χ. If $\chi < 0$, either ^{56}Ni dominates the makeup of the outer ejecta, or
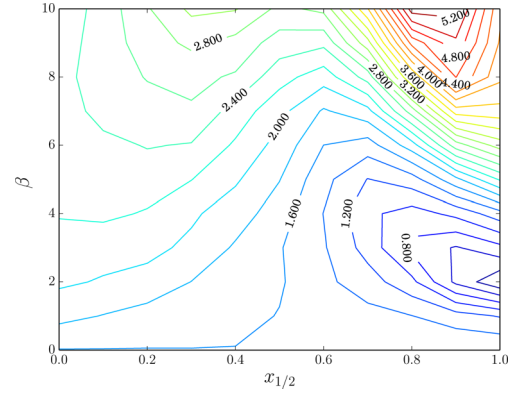

Figure 17. Contours showing the fitted n parameter of a bolometric light curve generated by using different values of β and $x_{1/2}$ in equation (5). A large range of n values are recovered, but extreme values of β and $x_{1/2}$ may not be physical.

the flux originates from elsewhere; potentially from some CSM interaction. Alternatively, the optical luminosity of the shock-heated cooling light curve may be dominant as this is expected to have $n = 1.5$. If $\chi \geq 0$, then the shock is not radiation pressure dominated and β may vary, or the delayed detonation transition model, from which the velocity gradient is calculated (Piro et al. 2010) is an incomplete description of this process. Other models, such as He double detonation (Fink et al. 2010) or the collision model (Kushnir et al. 2013; Dong et al. 2014) present different treatments of the velocity gradient.

More recent work (Piro & Nakar 2013) investigates the contribution of ^{56}Ni heating, both directly and from the diffusive tail, throughout the ejecta. In the appendices of Piro & Nakar (2013), rather than treating shells of material individually, integrals are evaluated over the entire ejecta. This leads to an altogether more complex picture of the energy generation, which depends on the relative fraction of ^{56}Ni throughout the ejecta, as given by

$$X_{56}(x) = \frac{1}{1 + \exp[-\beta(x - x_{1/2})]}, \qquad (5)$$

where x is a measure of depth within the ejecta, $x_{1/2}$ is the point at which the ^{56}Ni fraction is half at that of its value at peak, and β is the steepness of the rise in the distribution. Generating a bolometric luminosity using this parametrization, it is possible to attain a large range of n values, when fitting a power law (Fig. 17). The physical limits of this parameter space are uncertain, and fitting a number of SNe directly with this has yielded values in the ranges $6 \leq \beta \leq 8$ and $x_{1/2} \simeq 0.9$. The mean value of our study indicates that on average the envelope is less well mixed and there is an abrupt change within the ^{56}Ni distribution in most cases in the sample.

However, at very early times, fitting with a simple power law, the fit is poor, as the light curve is better described as an exponential (Piro & Nakar 2014). The time-scales for this discrepancy are short, and beyond the reach of this work. However, this may be the apparent 'break' in the power law seen in 2013dy and 2014J (Zheng et al. 2013, 2014) – an exponential rise turning into a power law at later times. Our finding that $\dot{n}$ is, in general, positive, supports this.

In Fig. 4 as the cutoff drops below ~ 3.5 d, n is consistent with 2, in agreement with Nugent et al. (2011). This value differs from our final result for SN 2011fe because the shorter time period used only probes a shallow region of the ejecta. At very early times, the rise index jumps to higher values. This difference could be hinting towards a broken power law as outlined in Section 2.1, equation (3),

or something that resembles one (Piro & Nakar 2014); however, attempting to fit this model to SN 2011fe is unsuccessful; as there is not enough data at very early times to constrain the seven free parameters.

At present, none of these various models make any predictions that would explain the decoupling of the early and late part of the rise seen in our data. However, a scatter in the measured photometric rise time can be explained by invoking a 'dark phase', between explosion and first light (Fig. 5), due to deep ^{56}Ni deposits. More work is needed to further understand this phenomena, using the methods previously applied to SN 2011fe and SN 2010jn (Hachinger et al. 2013; Mazzali et al. 2014), on future samples of well-observed SNe. The dark time for SN 2010jn was estimated to be 1.4 d, and that of SN 2011fe to be 1 d. As we expect that, for a given value of $x_{1/2}$, higher n values are consistent with a steeper gradient, β, higher n values should be consistent with a longer dark time. This effect is seen in these two SNe; SN 2011fe has an $n = 2.15 \pm 0.02$ [our value is used over that of Nugent et al. (2011) as the fitted regions are more comparable] and SN 2010jn $n = 2.3 \pm 0.6$.

As the available light curves can be well fitted by using a simple power law, more high-quality photometric and spectroscopic data are needed to distinguish between the models, and to see expected deviations from power laws (Zheng et al. 2013; Goobar et al. 2014). Ideally, future work would be able to concentrate on bolometric data, which is now becoming possible (Scalzo et al. 2014).

Tanaka et al. (2008) find a significant range of ^{56}Ni abundances in the outer ejecta of a sample of SNe Ia, which is taken as one of the causes of early time spectral variation in SNe Ia; they also suggest this could have photometric consequences. Our work clearly demonstrates that there is indeed a photometric shape variation, and that a cause of this is in ^{56}Ni deposition between SNe Ia, as suspected.

5.1 Type Ia 'CSM' supernovae

As considered in the previous subsection, one of the possible reasons for an SN to have an 'anomalous' rise would be an energy contribution from interaction with CSM material (Falk & Arnett 1977). Silverman et al. (2013) noted that the rise of SNe Ia-CSM tends to be significantly longer than a typical SNe Ia, following a simple photon diffusion argument – not only does a photon have to diffuse through the ejecta, but also significant amounts of CSM as well. In that respect, Ofek et al. (2014b) showed that in SNe IIn there is a possible correlation between rise time and peak luminosity.

We therefore examined PTF SNe Ia-CSM from the sample of Silverman et al. (2013) (7 SNe). Only three have sufficiently good photometry to provide acceptable fits, even after introducing constraints on the fitting. These fits assumed the fireball model, ($n = 2$), and the results of measuring the rise time can be seen in Fig. 18. One of these SNe, PTF12efc is a 'typical' broad and bright SNe-CSM, although having an extreme rise time and stretch, and seems to lie in agreement with the best fit to the distribution of normal SNe Ia. PTF10iuf also has a long rise and large stretch but a higher stretch than would be predicted from the measured rise time. Despite lying on or near the correlation of 'normal' SNe Ia, there seems to be no reason for this to be the case – the rise is shaped by different physical processes over different time-scales.

PTF11kx has a rise time of only $t_r^{n=2} = 14.5 \pm 0.2$ (Fig. 19), but a measured stretch of $s = 1.05$. In Dilday et al. (2012), a rise time of $\sim$20 d is assumed; note that a shorter rise time means that the ejecta will be smaller at a given epoch. Consequently, the ejecta mass calculated using the previous estimate ($\sim$5.3 M$_\odot$) is too large, and
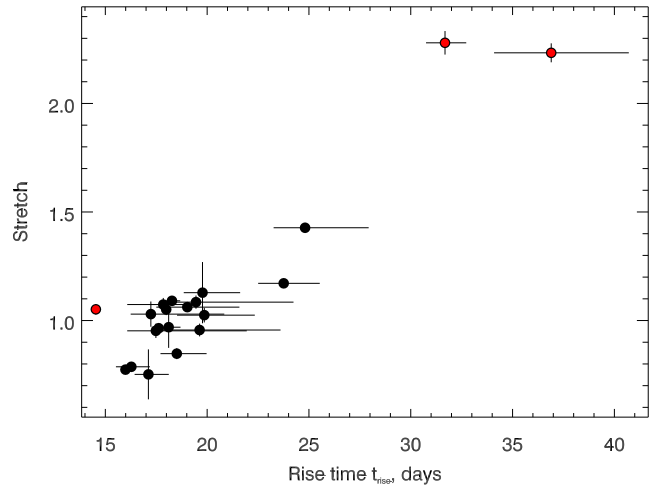

Figure 18. Stretch versus rise time with 3 SNe Ia identified as CSM by Silverman et al. (2013) plotted in red.
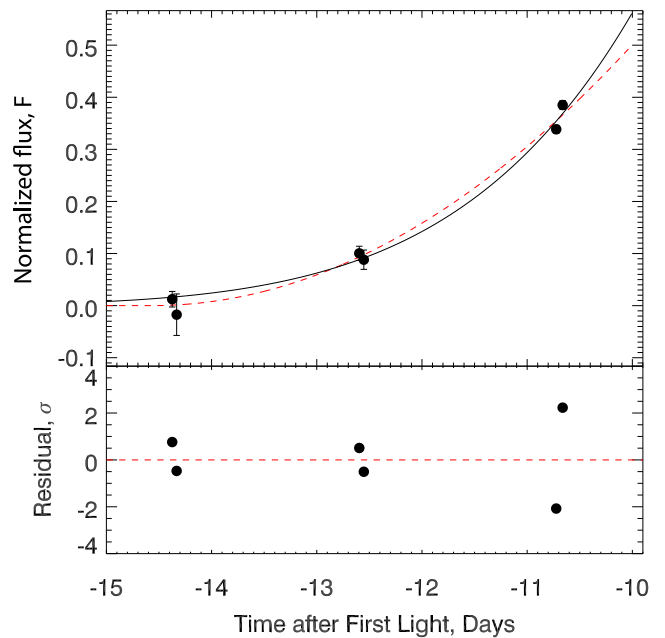

Figure 19. PTF11kx light curve and two fits to the data. A fit with fixed $n = 2$ is shown in red (dashed), and a fit with a fixed rise of $t_{\rm rise} = 20.0$ d is shown in black.

should be $\sim$80 per cent of that value, $\sim$4.3 M$_\odot$, making the same assumptions as in the supplemental information of Dilday et al. (2012). As well as performing a fit holding $n = 2$ a grid search was done to find the best fit where $t_r = 20$ d (Fig. 19). With a fixed rise, the best-fitting index was $n = 6.2 \pm 0.5$, this result is not physical for a 'normal' SN Ia, but SNe Ia-CSM have an additional contribution to their light from the collision of their ejecta with the CSM; this converts the kinetic energy in the ejecta into hard X-ray photons, which in the presence of sufficient optical depth can be converted into optical light (e.g. Chevalier & Irwin 2012; Svirski, Nakar & Sari 2012; Ofek et al. 2014b). With this in mind, it may be expected for SNe Ia-CSM to have abnormal rise properties. Until a confirmed SN Ia-CSM is observed with enough precision to enable a relaxing of n, few constraints can be placed on the effect of CSM on a rising light curve.

6 CONCLUSIONS

In this work, we have used 18 SNe Ia from the PTF and the LSQ to measure the rise time ($t_{\rm rise}$) (the time between first light t_0 and maximum light $t_{\rm max}$) and rise index (n), where $f = (t - t_0)^n$. Our main conclusions are as follows.

(i) The rise index, n, of our sample shows significant variation ($1.48 \leq n \leq 3.70$), with the mean of the distribution $n = 2.44 \pm 0.13$ and $n = 2.5 \pm 0.13$ when correcting to a pseudo-bolometric value (Section 4.2), both inconsistent with a simple fireball model ($n = 2$) at a 3σ level. This implies that current understanding of the ^{56}Ni distribution or shock velocity through the ejecta is incomplete, and that more complex physically motivated parametrizations may be needed in future.

(ii) We find that when the rise index is allowed to vary with time from $n = 2$, $\dot{n}$ is in general positive, with an average value of $\dot{n} = 0.011 \pm 0.004 \, {\rm d}^{-1}$. Supporting a time dependant, n, is the finding that SN discovered later after first light have, in general, a larger value of n, whereas those discovered soonest after t_0 have lower values.

(iii) The average $t_{\rm rise}$ of our sample is $t_{\rm rise} = 18.98 \pm 0.54$ d, and $t_{\rm rise} = 18.97 \pm 0.43$ d, when correcting for light-curve width. We find no evidence for two rise-time modes in our sample. These are longer than would ordinarily be found by enforcing $n = 2$.

(iv) The broadest light curves have a $t_{\rm rise}$ that is faster than that of our stretch-corrected light-curve template, which enforces $n = 2$ in its construction. In agreement with previous studies, we find that a 'two-stretch' model fits the data better. In contrast to current two-stretch fitting methods, which separate the light curve into the pre- and post-maximum sections ($t < t_{\rm max}$ and $t > t_{\rm max}$, respectively), the most significant variation occurs at the very earliest epochs ($t < t_{0.5}$, where $t_{0.5}$ is the time at which the SNe reaches half of its maximum, or phases $\tau < -10$ d).

(v) We therefore decouple the rise time into two components: t_1 (where $t_1 = t_{0.5} - t_0$) and t_2 (where $t_2 = t_{\rm max} - t_{0.5}$). These time-scales are not correlated with each other (Fig. 11); furthermore t_2 is strongly correlated with stretch, whereas t_1 is not. As a result, stretch-correcting using a single stretch is ineffective in reducing the dispersion in the earliest portion of the light curve (Fig. 13).

(vi) These two regions are separated by the approximate location of the point at which energy deposition and radiation are equal, meaning that the physical conditions are distinct.

(vii) Using models from Piro & Nakar (2013), we show that potential variation in the shape of the ^{56}Ni distribution within the SN ejecta can explain the measured range of n and $t_{\rm rise}$.

(viii) SNe Ia showing evidence of strong interaction with CSM have long rise times. However a notable member of this subclass, PTF11kx, has an extremely short rise, $t_{\rm rise} = 14.5 \pm 0.5$ d, when fitted with a fireball model ($n = 2$).

Further work should concentrate on further understanding the variation, and on which other observable quantities it depends. For this, a large sample of SNe Ia with high-quality photometric and spectroscopic data must be assembled. The presence of high-velocity features, Si II velocities and colour evolution may hold valuable information, particularly if the variation at very early times is misunderstood when used for cosmology.

REFERENCES

Ahn C. P. et al., 2014, ApJS, 211, 17
Arnett W. D., 1982, ApJ, 253, 785
Astier P. et al., 2006, A&A, 447, 31
Baltay C. et al., 2007, PASP, 119, 1278
Baltay C. et al., 2013, PASP, 125, 683
Betoule M. et al., 2014, A&A, 568, A22
Bianco F. et al., 2011, ApJ, 741, 20
Bloom J. S. et al., 2012, ApJ, 744, L17
Bramich D. M., 2008, MNRAS, 386, L77
Chevalier R. A., Irwin C. M., 2012, ApJ, 747, L17
Colgate S. A., McKee C., 1969, ApJ, 157, 623
Conley A. et al., 2006, ApJ, 132, 1707
Conley A. et al., 2008, ApJ, 681, 482
Conley A. et al., 2011, ApJS, 192, 1
Dilday B. et al., 2012, Science, 337, 942
Dong S., Katz B., Kushnir D., Prieto J. L., 2014, preprint (arXiv:1401.3347)
Faber S. M. et al., 2003, in Iye M., Moorwood A. F. M., eds, SPIE Conf. Ser. Vol. 4841, Instrument Design and Performance for Optical/Infrared Ground-based Telescopes. SPIE, Bellingham, p. 1657
Falk S. W., Arnett W. D., 1977, ApJS, 33, 515
Fink M., Röpke F. K., Hillebrandt W., Seitenzahl I. R., Sim S. A., Kromer M., 2010, A&A, 514, A53
Frieman J. A. et al., 2008, AJ, 135, 338
Ganeshalingam M., Li W., Filippenko A., 2011, MNRAS, 416, 2607
González-Gaitán S. et al., 2012, ApJ, 745, 44
Goobar A. et al., 2014, ApJ, 784, L12
Guy J. et al., 2007, A&A, 466, 11
Guy J. et al., 2010, A&A, 523, A7
Hachinger S. et al., 2013, MNRAS, 429, 2228
Hayden B. et al., 2010a, ApJ, 712, 350
Hayden B. T. et al., 2010b, ApJ, 722, 1691

Henden A. A., Welch D. L., Terrell D., Levine S. E., 2009, Am. Astron. Soc. Meeting Abstr., #214, #407.02
Hook I. M., Jørgensen I., Allington-Smith J. R., Davies R. L., Metcalfe N., Murowinski R. G., Crampton D., 2004, PASP, 116, 425
Hoyle F., Fowler W. A., 1960, ApJ, 132, 565
Hsiao E. Y., Conley A., Howell D. A., Sullivan M., Pritchet C. J., Carlberg R. G., Nugent P. E., Phillips M. M., 2007, ApJ, 663, 1187
Iben I., Jr, Tutukov A. V., 1984, ApJS, 54, 335
Kasen D., 2010, ApJ, 708, 1025
Katz B., Dong S., 2012, preprint (arXiv:1211.4584)
Kessler R. et al., 2009, ApJS, 185, 32
Kushnir D., Katz B., Dong S., Livne E., Fernández R., 2013, ApJ, 778, L37
Laher R. R. et al., 2014, PASP, 126, 674
Lantz B. et al., 2004, in Mazuray L., Rogers P. J., Wartmann R., eds, SPIE Conf. Ser. Vol. 5249, Optical Design and Engineering. SPIE, Bellingham, p. 146
Law N. et al., 2009, PASP, 121, 1395
Li W. D. et al., 2000, in Holt S. S., Zhang W. W., eds, AIP Conf. Ser. Vol. 522, The Lick Observatory Supernova Search. Am. Inst. Phys. New York, p. 103
Livne E., Arnett D., 1995, ApJ, 452, 62
Maguire K. et al., 2012, MNRAS, 426, 2359
Maguire K. et al., 2014, MNRAS, 444, 3258
Maoz D., Mannucci F., Nelemans G., 2014, ARA&A, 52, 107
Mazzali P. A. et al., 2014, MNRAS, 439, 1959
Miller J. S., Stone R. P. S., 1994, Technical Report 66, The Kast Double Spectograph. University of California Observatories/Lick Observatory
Nakar E., Sari R., 2012, ApJ, 747, 88
Nugent P. E. et al., 2011, Nature, 480, 344
Ofek E. O. et al., 2012a, PASP, 124, 62
Ofek E. O. et al., 2012b, PASP, 124, 854
Ofek E. O. et al., 2013, Nature, 494, 65
Ofek E. O. et al., 2014a, ApJ, 781, 42
Ofek E. O. et al., 2014b, ApJ, 788, 154
Oke J. B. et al., 1995, PASP, 107, 375
Pakmor R., Kromer M., Taubenberger S., Sim S. A., Röpke F. K., Hillebrandt W., 2012, ApJ, 747, L10
Pan Y.-C. et al., 2014, MNRAS, 438, 1391
Parrent J. T. et al., 2012, ApJ, 752, L26
Patat F. et al., 2007, Science, 317, 924
Pereira R. et al., 2013, A&A, 554, A27
Perlmutter S. et al., 1997, ApJ, 483, 565
Perlmutter S. et al., 1999, ApJ, 517, 565
Phillips M. M., 1993, ApJ, 413, L105
Pinto P. A., Eastman R. G., 2000a, ApJ, 530, 744
Pinto P. A., Eastman R. G., 2000b, ApJ, 530, 757
Piro A. L., 2012, ApJ, 759, 83
Piro A. L., Nakar E., 2013, ApJ, 769, 67
Piro A. L., Nakar E., 2014, ApJ, 784, 85
Piro A. L., Chang P., Weinberg N. N., 2010, ApJ, 708, 598
Pskovskii Y. P., 1984, SvA, 28, 658
Rabinak I., Livne E., Waxman E., 2012, ApJ, 757, 35
Rau A. et al., 2009, PASP, 121, 1334
Rest A. et al., 2014, ApJ, 795, 44
Riess A. G., Press W. H., Kirshner R. P., 1996, ApJ, 473, 88
Riess A. G. et al., 1998, ApJ, 116, 1009
Riess A. G. et al., 1999, AJ, 118, 2675
Scalzo R. et al., 2014, MNRAS, 440, 1498
Shen K. J., Bildsten L., 2014, ApJ, 785, 61
Silverman J. M. et al., 2013, ApJS, 207, 3
Strovink M., 2007, ApJ, 671, 1084
Sullivan M. et al., 2011, ApJ, 737, 102
Suzuki N. et al., 2012, ApJ, 746, 85
Svirski G., Nakar E., Sari R., 2012, ApJ, 759, 108
Tanaka M. et al., 2008, ApJ, 677, 448
Whelan J., Iben I., Jr, 1973, ApJ, 186, 1007
Woosley S. E., Weaver T. A., 1994, ApJ, 423, 371
Woosley S. E., Kasen D., Blinnikov S., Sorokina E., 2007, ApJ, 662, 487
Yaron O., Gal-Yam A., 2012, PASP, 124, 668
York D. G. et al., 2000, AJ, 120, 1579
Zheng W. et al., 2013, ApJ, 778, L15
Zheng W. et al., 2014, ApJ, 783, L24

SUPPORTING INFORMATION

Additional Supporting Information may be found in the online version of this article:

Table 2. Table of example data for one SN, PTF09dsy (http://mnras.oxfordjournals.org/lookup/suppl/doi:10.1093/mnras/stu2314/-/DC1).

Please note: Oxford University Press are not responsible for the content or functionality of any supporting materials supplied by the authors. Any queries (other than missing material) should be directed to the corresponding author for the paper.

This paper has been typeset from a TEX/LATEX file prepared by the author.